Synthesis, characterization and magnetic properties of halogenated tetranuclear cubane-like nickel(II) complexes

Mahnaz Aryaeifar,[a] Hadi Amiri Rudbari, *[a] Eufemio Moreno-Pineda,[bc] José V. Cuevas-Vicario, [d] Sagar Paul, [e] Michael Schulze, [e] Wolfgang Wernsdorfer, *[efg] Francisco Lloret,[h] Nakisa Moini[i] and Olivier Blacque [j]

Four Ni_4O_4 cubanes with formula $[Ni_4(Cl_2\text{-}L)_4(\mu_3\text{-}OMe)_4(MeOH)_4]$ (**1**), $[Ni_4(Br_2\text{-}L)_4(\mu_3\text{-}OMe)_4(MeOH)_4]$ (**2**), $[Ni_4(I_2\text{-}L)_4(\mu_3\text{-}OMe)_4(MeOH)_4]$ (**3**) and $[Ni_4(BrCl\text{-}L)_4(\mu_3\text{-}OMe)_4(MeOH)_4]$ (**4**) (Cl_2-LH = 3,5-dichlorosalicylaldehyde, Br_2-LH = 3,5-dibromosalicylaldehyde, I_2-LH = 3,5-diiodosalicylaldehyde, BrCl-LH = 3-bromo-5-chlorosalicylaldehyde) were obtained by self-assembly from commercially available 3,5-halogen-substituted salicylaldehydes and $NiCl_2{\cdot}6H_2O$ in high yields at room temperature. The X-ray crystal structure analysis of **4** showed a cubane-type structural topology as each Ni(II) ion is six-coordinated in a distorted octahedral geometry defined by four oxygen atoms from the MeOH molecule (three as bridging methoxy-oxygens and one as terminal group) and two oxygen atoms from the 3-bromo-5-chlorosalicylaldehyde ligands. The cubane core is stabilized *via* an intramolecular O–H···O hydrogen bond, while in the crystal, complex molecules are linked into the zigzag chain to the *a*-axis *via* strong Br···Br interaction. Both SQUID and μSQUID measurements indicate the coexistence of ferromagnetic and antiferromagnetic interactions in two complexes. The fitting of the magnetic data yields different magnetic parameters for each complex, clearly highlighting the differences in the magnetic properties among these systems. DFT calculations have also been performed on compounds **1–4** to explain the exchange interaction mechanisms between the Ni(II) ions, supporting both the magnitude and sign of the coupling constants.

1. Introduction

Polynuclear metal complexes have become a major area of study over the last 20 years. The interests in these clusters span from pure academic aspects of chemistry to potential applications as functional materials in biological systems,[1,2] catalysis[3,4] and molecular magnetism.[5–10] Among them, cubane-type $\{M_4O_4\}$ clusters [M(II) = Cu, Ni, Co, *etc.*] have attracted a renewed interest, especially for magnetic properties.[11–15] The tunability of magnetic exchange between paramagnetic metal ions is important not only from a theoretical point of view,[16] which aims to understand the fundamental correlation between the structure and magnetic properties but also targets the development of single-molecule magnets (SMMs) for versatile applications.[17–23]

[a] *Department of Chemistry, University of Isfahan, Isfahan 281746-73441, Iran. E-mail: h.a.rudbari@sci.ui.ac.ir, hamiri1358@gmail.com*
[b] *Universidad de Panamá Facultad de Ciencias Naturales, Exactas y Tecnología, Depto. de Química-Física, Panama*
[c] *Universidad de Panamá Facultad de Ciencias Naturales, Exactas y Tecnología, Grupo de Investigación de Materiales, Panama*
[d] *Departamento de Química, Universidad de Burgos, Pza. Misael Bañuelos S/N, Burgos, Spain*
[e] *Physikalisches Institut, Karlsruhe Institute of Technology, D-76131 Karlsruhe, Germany. E-mail: wolfgang.wernsdorfer@kit.edu*
[f] *Institute for Quantum Materials and Technology (IQMT), Karlsruhe Institute of Technology (KIT), Hermann-von-Helmholtz-Platz 1, D-76344 Eggenstein-Leopoldshafen, Germany*
[g] *Institute for Quantum Materials and Technology (IQMT), Karlsruhe Institute of Technology (KIT), Hermann-von-Helmholtz-Platz 1, D-76344 Eggenstein-Leopoldshafen, Germany*
[h] *Departament de Química Inorganica/Instituto de Ciencia Molecular (ICMol), Universitat de Valencia, C/Catedrático José Beltran 2, 46980 Paterna, València, Spain*
[i] *Department of Chemistry, Faculty of Physics and Chemistry Alzahra University, P.O. Box 1993891176, Vanak Tehran, Iran*
[j] *Department of Chemistry, University of Zurich, Winterthurerstrasse 190, CH-8057, Zurich, Switzerland*

In these cubane cages, the interaction between two paramagnetic metal centers is mediated by μ_3-O bridges originating from –OH, –OMe, or a chelating ligand.[24 29]

The most important parameter to govern the sign and magnitude of exchange interaction of the M_4O_4 cubane cores is the M–O–M angle; for example, it has been shown that the Ni_4O_4 core exhibits ferromagnetic interactions when the Ni–O–Ni angle is less than 98° and antiferromagnetic interactions when the angle is greater than 109°.[30 32] However, recently many different directions have been pursued in the research field of SMMs,[33 45] in which an important direction is to explore the effects of ligand substitution.[10,46]

On the other hand, it is found that the relaxation of magnetization in a SMM could be tuned by electronic effects on its ligand set. Indeed, two binuclear phenoxo-bridged [Dy – radical] compounds were synthesized and despite the same structure, the presence of the Br substituent was found to have a dramatic effect on the AC susceptibility behavior.[47] Also, some studies have revealed that halogen atoms substantially influence magnetization dynamics. These atoms which are electronegative elements could be influencing the strength of the magnetic exchange interaction,[48] which have previously been shown to directly influence the anisotropy barrier and thus the relaxation time.[49] Several factors affecting the magnetic properties of the cluster were investigated to explore ways to improve the SMM properties. An instance of studies in this field has shown that the presence of halogen atoms through supramolecular interaction between molecules influences the anisotropy of metals, which leads to different blocking temperatures (T_B).[10]

Recent studies show that halogen atoms have a good potential to improve SCO properties due to their high ability in the formation of intermolecular interactions (halogen bond) as well as electronic effects.[50 53] The halogen bond occurs when there is evidence of a net attractive interaction between an electrophilic region associated with a halogen atom in a molecular entity and a nucleophilic region in another, or the same, molecular entity. Halogen atoms undergo three kinds of weak non-covalent interactions, specifically halogen bonding, halogen–halogen interactions, and halogen–π interactions. Based on the geometry, halogen···halogen interactions are known to be of two types, type 1 and type 2.[54] Aiming to understand the role of halogen atoms in magnetic properties of cubane-type $\{M_4O_4\}$ clusters, here, a number of cubane-type $\{Ni_4O_4\}$ clusters with 3,5-substituted-2-hydroxybenzaldehyde were synthesized and their magnetic properties were investigated (Scheme 1).

2. Results and discussion

2.1. Synthesis and general characterization

Tetranuclear cubane-like Ni(II) complexes, **1–4**, in high yields were prepared by the reaction of $NiCl_2{\cdot}6H_2O$ with methanolic solutions of halogen-substituted salicylaldehyde as chelating ligands in the presence of triethylamine at room temperature (Scheme 1).

The IR spectra show broad peaks at ~3350 cm^{-1} for all complexes due to the presence of OH group of the methanol molecule in all structures, while the $\nu(C–O_{phen})$ stretching mode occurs as a very strong band at ~1150 and alcoholic C–O stretches as a peak at 1041 cm^{-1},[55] Several weak peaks observed in the range 3000–2760 cm^{-1} and are attributed to the aromatic and aliphatic C–H stretches (Fig. S1, ESI†).

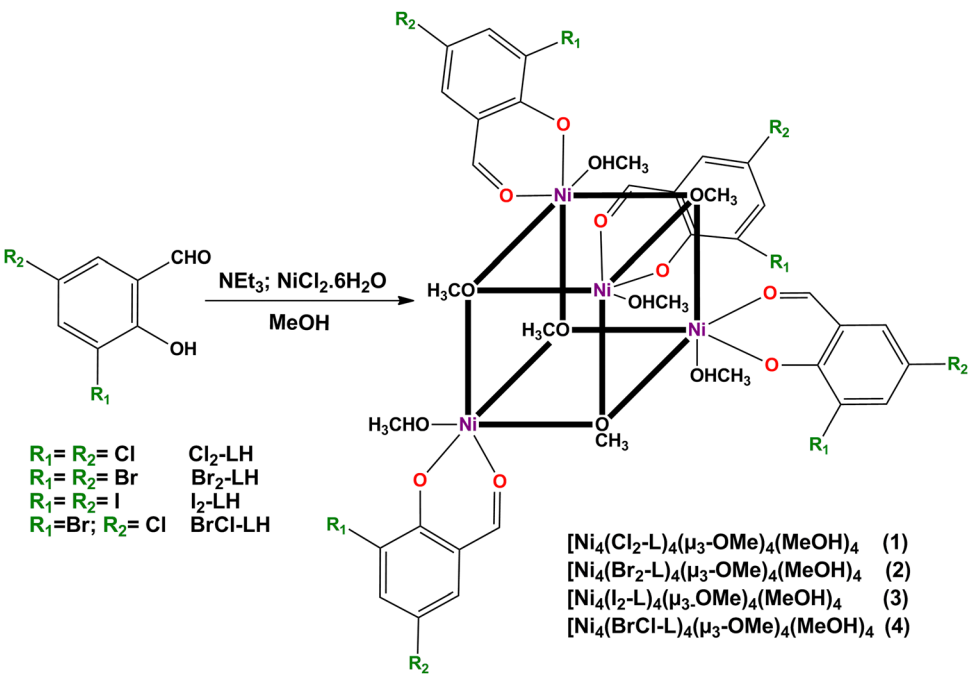

Scheme 1 Overview of the synthesis and topology of complexes.

2.2. Crystal structures of $[Ni_4(BrCl\text{-}L)_4(\mu_3\text{-}OMe)_4(MeOH)_4]$ (4)

Single crystal X-ray structure analysis reveals that **4** crystallizes in the monoclinic system space group $P2_1/c$. Crystallographic data and parameters for compound **4** are given in Table S1 (ESI†), while, selected bond distances and angles are listed in Table S2 (ESI†). As shown in Fig. 1, four Ni atoms and four O atoms, each from MeO , occupy alternate corners of the cubane unit where each Ni atom is surrounded by three bridging O atoms derived from MeO , one from MeOH and two O atoms from chelating ligand leading to a distorted octahedral geometry (Fig. 2a). The bond lengths are in the range of 1.991(5)–2.153(6) Å (average value 2.0497 Å). Looking down the *b*-axis, the cubane core is slightly distorted; the top face is faintly rotated in comparison with the bottom face (Fig. 2b). A tetrahedron structure with Ni···Ni separations being in the range of 3.0332(15)–3.1001(15) Å is generated by linking the adjacent Ni(II) centers (Fig. 2c). The tetranuclear core is bridged solely by μ_3-methoxide groups resulting in one unique exchange pathway between the metal centers. Each of the bridging oxygen atoms has a remarkably distorted tetrahedral geometry (Fig. 2d). The Ni–O(MeOH) bond lengths are longer than those for Ni–O(MeO).

It has been shown that the Ni(II) core exhibits ferromagnetic interactions when the Ni–O–Ni angle is less than 98° and antiferromagnetic interactions when the angle is greater than 109°.[30 32] All the bond angles (Ni–O–Ni and O–Ni–O) of the cubane in **4** are close slightly smaller than 98°, except for Ni(3)–O(9)–Ni(4) (99.0(2)°). The *trans* O–Ni1–O and Ni–O–Ni angles cover the ranges 166.60(8)–177.83(9)° and 166.60(8)–177.83(9)°, respectively.

The cubane units are well isolated from each other, the centroid–centroid distance between adjacent $\{Ni_4O_4\}$ entities along the crystallographic *a*, *b*, *c* axes are 9.079, 15.037 and 15.396 Å, respectively. Similar to what was observed in the previously published $[Ni_4L_4(solv)_4]$ compounds, the four exogenous MeOH ligands serve as hydrogen bond donors toward the phenolate oxygen. Thus, four faces of the $\{Ni_4O_4\}$ cube (denoted as side faces, SF) are spanned by O–H···O hydrogen bonds, while the two remaining faces, which are located at opposite sides of the cube (denoted OF and colored in blue in Fig. 3), are not bridged. This leads to distinct bond lengths and angles for the two different types of cube faces SF and OF (Table S2, ESI†). In particular, bond angles at the bridging oxygen atoms are significantly more acute along the faces spanned by O–H···O hydrogen bonds (SF), resulting in shorter Ni···Ni distances and deformation of the cubane core away from ideal cubic symmetry. Thus, the complex displays approximate S_4 site symmetry, while the exact crystallographic point symmetry is C_1. These differences, primarily in the bridging Ni–O–Ni angles (Table S2, ESI†), are crucial factors that determine the sign of the magnetic exchange interactions through O-atom bridges; their modulation has drastic effects on the ground state of the complexes.

In the crystal packing, the molecules pack in a herringbone arrangement along the *a*-axis, and stack in an eclipsed manner down the *c*-axis (Fig. 4). A zigzag chain of Br atoms is visible when viewed down the *a*-axis and involves a short Br···Br contact of 3.5013(17) Å. Based on the distance (Br(2)···Br(4) = 3.5013(17) Å) and angles (C(16)–Br(4)···Br(2) = 145.867° and C(9)–Br(2)···Br(4) = 137.164°) in Br···Br contacts, the halogen–halogen interactions

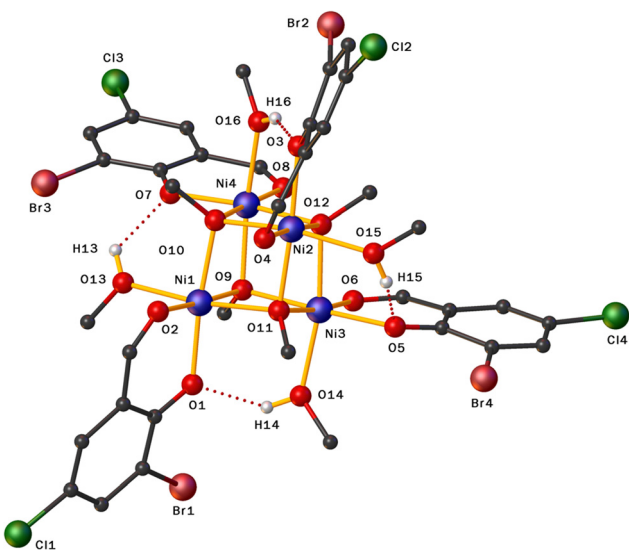

Fig. 1 Molecular structure of $[Ni_4(BrCl\text{-}L)_4(\mu_3\text{-}OMe)_4(MeOH)_4]$ (**4**). Hydrogen atoms (except those involved in hydrogen bonding interactions) have been omitted for clarity. Hydrogen bonds are represented by dashed lines. Color code: Ni, blue; O, red; C, black; Cl, green; Br, dark red.

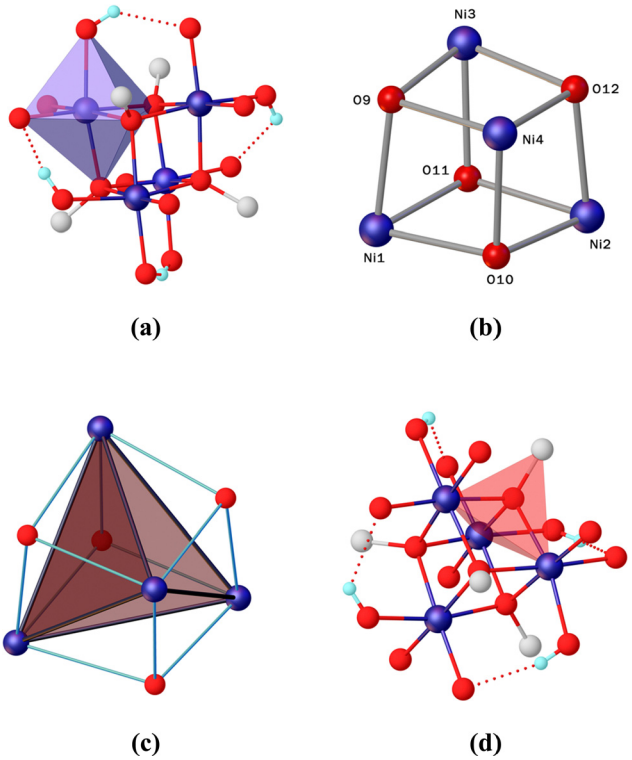

Fig. 2 (a) Coordination polyhedron at each Ni(II) ion (b) cubane-type $\{Ni_4O_4\}$ core; (c) and (d) environment of each bridged oxygen atom in $[Ni_4(BrCl\text{-}L)_4(\mu_3\text{-}OMe)_4(MeOH)_4]$ (**4**). Color code: Ni, blue; O, red; C, gray; H, light blue.

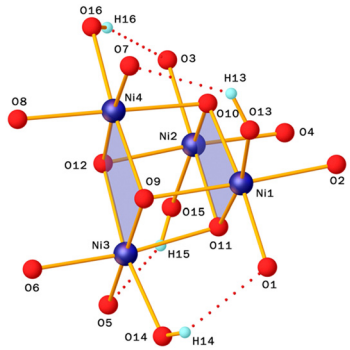

Donor—H....Acceptor	D—H/Å	H…A/Å	D…A /Å	D – H…A/°
O(13)—H(13)…O(7)	0.86(2)	2.22(6)	2.822(9)	128(6)
O(14)—H(14)…O(1)	0.86(3)	2.19(7)	2.790(8)	127(6)
O(15)—H(15)…O(5)	0.85(7)	2.10(7)	2.850(9)	148(5)
O(16)—H(16)…O(3)	0.87(9)	2.00(9)	2.799(9)	153(12)

Fig. 3 Emphasis of the cubane-like $\{Ni_4O_4\}$ fragment and hydrogen bonding interactions in $[Ni_4(BrCl\text{-}L)_4(\mu_3\text{-}OMe)_4(MeOH)_4]$ (**4**). Blue faces (OF) are not spanned by hydrogen bonds.

can best describe as type II.[54,56] Non-classical hydrogen bonds and other intermolecular interactions with distances shorter than the sum of van der Waals radii are shown in Table S3 (ESI†).

Supramolecular packing in complex **4**, as mentioned above, is further supported by the analyses of intermolecular interactions with the Hirshfeld surfaces using the program CrystalExplorer.[57 61] The Hirshfeld surfaces with d_{norm} properties, fingerprint plots and percentages of contributions to various types of contacts in the fingerprint plots are illustrated in Fig. 5.

As shown in Fig. 5, supramolecular packing analyses for complex **4** show different kinds of intermolecular interactions such as halogen···halogen, halogen···carbon, halogen···hydrogen, carbon···hydrogen and hydrogen···hydrogen. Because of the Br and Cl halogen atoms as substituents on the salicylaldehyde ligand, most of the strong intermolecular interactions are between these halogen atoms and other atoms. As shown in Fig. 5, the chlorine and bromine intermolecular contacts (X···X, X···C and X···H, X···O) cover 48% of the whole Hirshfeld surface. This high contribution of intermolecular interactions for halogen atoms can be attributed to the relatively large vdW radius of halogen atoms.

Hirshfeld surface analyses indicate the stronger intermolecular interactions between two molecules at a distance shorter than the sum of the vdW radii as red spots on the d_{norm} surfaces (Fig. 5). These strong intermolecular interactions are Br···Br, Br···H, and Cl···H, which cover 42% of the whole Hirshfeld surface (Fig. 5).

Among these interactions, the strongest one is observed for Br···Br with the lowest contribution (1%). The van der Waals radii (vdW) for the Br atom is 1.87 Å and the corresponding sum of the van der Waals radii for Br + Br = 3.74 Å,[61] while the length of this intermolecular interaction in complex **4** is 3.5013(17) Å, which is clearly shorter than the sum of van der Waals radii of two Br atoms.

The bar chart in Fig. 5 illustrates that the highest contribution to the Hirshfeld surfaces is due to the H-atom interactions with other atoms such as halogen (Br···H and Cl···H), oxygen (O···H), carbon (H···C), and hydrogen (H···H). These contacts contribute to nearly 90% of the total Hirshfeld surface area. Also, it is worth noting that except the Br···Br interaction, all other strong interactions identified in Hirshfeld surfaces map are between hydrogen atoms with other atoms (Br···H, Cl···H and H···H).

2.3. Magnetic studies

Magnetic studies of complexes **1** to **4** were carried out on powdered samples in a SQUID magnetometer. Fig. 6 shows the magnetic behavior of the thermal variation of the $\chi_M T$ product (χ_M is the molar magnetic susceptibility corrected for the diamagnetism) under an applied field of 1 kOe. As depicted, the room temperature $\chi_M T(T)$ is 5.43, 5.48, 5.61 and 5.47 cm^3 mol^{-1} K for **1**, **2**, **3** and **4**, respectively. The $\chi_M T(T)$ is in the range of Ni(II) complexes (*i.e.*, for $S = 1$ and $g > 2.00$). Upon cooling, $\chi_M T$ increases slightly to *ca.* 100 K, where it abruptly increases to a maximum of 10.28 cm^3 mol^{-1} K at 9 K for **1**, while for **2**, **3** and **4** values of 12.05, 11.83 and 10.65 cm^3 mol^{-1} K are observed at 14 K, respectively. The upsurge present in all cases highlights the presence of ferromagnetic interactions operating within the Ni_4 cage.[62 66] Magnetization *versus* field studies show the highest $M(H)$ values at the highest field (5 T) and lowest temperature (2 K) of 8.8, 8.9, 9.8 and 8.5 N_β for **1**, **2**, **3** and **4**, respectively (see insets in Fig. 6).

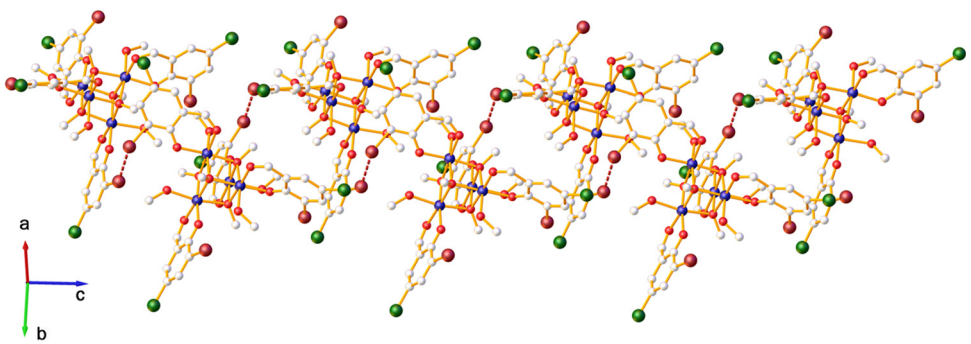

Fig. 4 Br···Br interactions in complex **4**.

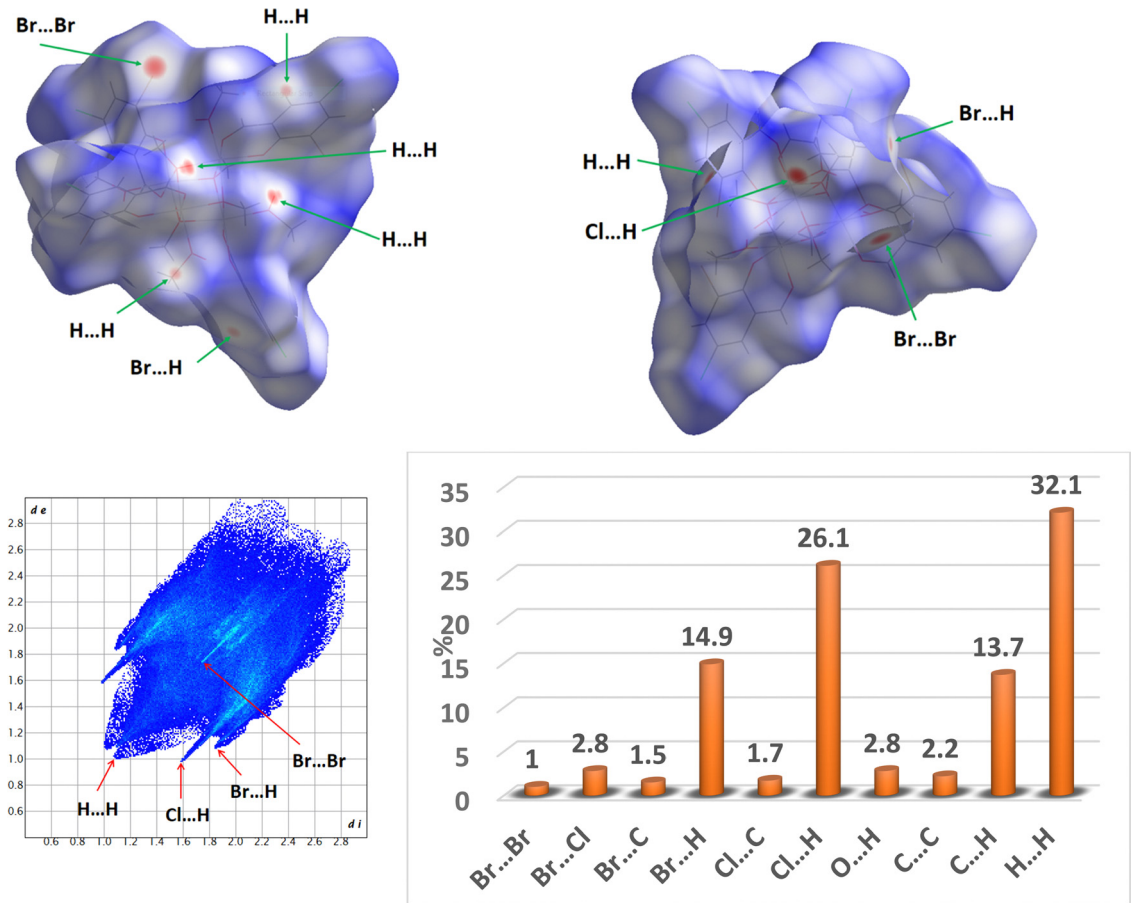

Fig. 5 Hirshfeld surfaces mapped with d_{norm} properties (up) and fingerprint plot (left down) for complex **4**. Red spots represent the closest contacts and blue the most distant contacts. ESP (electrostatic potential) plotted on Hirshfeld surfaces mapped from −0.1810 au (red) to 1.6179 au (blue). Right down: relative contributions to the Hirshfeld surfaces area for different inter and interamolecular contacts in complex **4**.

Considering the crystal structure of the Ni_4 cage, two interaction pathways were considered,[62 66] to simultaneously fit the $\chi_M T(T)$ and $M(H,T)$ in PHI.[67] A Hamiltonian of the following form was employed:

$$\begin{aligned}\mathcal{H} &= -2J_1(S_{Ni1}S_{Ni2} + S_{Ni2}S_{Ni3} + S_{Ni3}S_{Ni4}) \\ &\quad -(S_{Ni1}S_{Ni3} + S_{Ni2}S_{Ni4}) \\ &\quad + D_{Ni}\sum_{i=1}^{4}[S_{zi}{}^2 - S(S+1)/3]\end{aligned} \quad (1)$$

where the first and second terms are the exchange interaction between the closest Ni(II) ions and the third term is the zero-field splitting parameter. For **1**, the best fit yields J_1 = +9.3(6) cm^{-1}, J_2 = −0.4(7) cm^{-1}, D_{Ni} = −1.79(3) cm^{-1}, g = 2.190(1) and zJ = 5.54(4) × 10^{-3} cm^{-1} with R = 5.4 × 10^{-5} (with $R = \sum_{i}^{points}\left[M_{exp} - M_{calc}\right]^2$). For **2**, the following parameters were obtained: J_1 = +6.27(9) cm^{-1}, J_2 = +6.26(2) cm^{-1}, g = 2.217(5) with R = 0.6047, while for **3** the best fits yields: J_1 = +12.5(2) cm^{-1}, J_2 = +1.94(2) cm^{-1}, D_{Ni} = −1.13(6) cm^{-1}, g = 2.182(9), zJ = 7.9(1) × 10^{-4} cm^{-1} with R = 3.23. In contrast to the fits for complexes **1–3**, the fit for $M(H,T)$ data for **4** is rather poor (especially at high fields), indicating that more than two exchange pathways might be operative and/or strong intermolecular interactions. Inclusion of the rhombic term (E) did not improve the fits. The best fit for **4** yields the following parameters: J_1 = +32.5(3) cm^{-1}, J_2 = −18.8(2) cm^{-1}, D_{Ni} = +0.05(9) cm^{-1}, g = 2.083(1), zJ = 4.7(1) × 10^{-3} cm^{-1} with R = 15.7. The first clearly highlights important differences between all complexes, *e.g.*, while for **1** and **3** important anisotropy is expected due to the sign and magnitude of the zero-field splitting parameter, negligible anisotropy is expected for **2** and **4**.

To further investigate the magnetic anisotropy of the complexes, μSQUID studies were carried out at sub-Kelvin temperatures. The studies were carried out on micrometer-sized single crystals, with the field aligned along the easy crystallographic axis. As shown in Fig. 7, the loops are rather narrow for all complexes. For **1** and **3** a small opening is observed between ±0.4 T, indicative of small magnetic anisotropy. In contrast, for **2** and **4** the loops are almost closed at the lowest temperature and fastest sweeping rate (*i.e.*, 30 mK and 0.128 T s^{-1}). The μSQUID results are in agreement with the parameters obtained from $\chi_M T(T)$ and $M(H,T)$ in which larger D parameters were obtained for **1** and **3**. Unfortunately, the lack of crystal

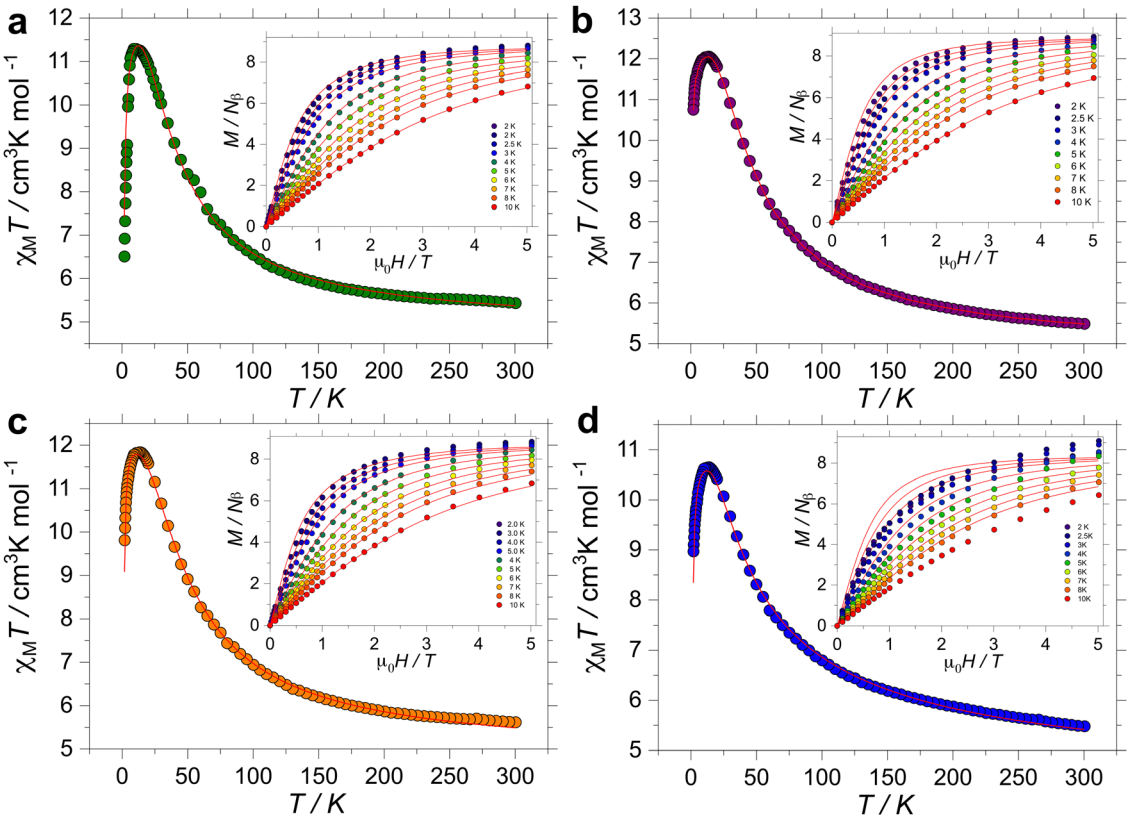

Fig. 6 Magnetic susceptibility ($\chi_M T(T)$) data for complexes **1–4**, magnetization ($M(H)$) (insets) and fits (solid red traces) employing the parameters described in the text. $\chi_M T(T)$ and $M(H)$ data (a) for **1**; (b) **2**; (c) **3** and (d) **4**.

structures of these complexes precludes detailed analysis of the μSQUID loops. However, the high-temperature data as well as the sub-Kelvin temperature loops show some of the important variations between the four complexes.

Apart from larger anisotropy in complexes **1** and **3**, indicated by the opening of the μSQUID loops, complexes **1** and **4** have certain similarities in the type of exchange interaction. Both the SQUID and μSQUID data suggest a coexistence of ferromagnetic (FM) and an antiferromagnetic (AFM) interaction in these two compounds. In the fitting of SQUID data, this results in two exchange interactions $J_{1,2}$ with different signs and in the μSQUID loop it results in three peaks in dM/dH at $\pm B_{ex}$ and B = 0 fields (Fig. 7a, d and e). The derivative-field map (Fig. 7f) obtained from angle-dependent μSQUID $M(H)$ loops in compound **4** elucidates this fact. A 3D vector magnet equipped with the μSQUID setup allows angle dependent $M(H)$ measurements with an angular precision better than 0.1° without manually rotating the sample. The derivatives dM/dH in complex **4**, from experimental $M(H)$ curves (positive cycle) measured at different angles of external field, are mapped with direction of applied field (H_x, H_y). The observed parallel lines in Fig. 7f indicate the switching fields between AFM to FM states. Only one pair of lines would suggest a single easy axis for the AFM ordering. However, here two sets of parallel lines are observed, suggesting two AFM axis, and a strong derivative about zero field along x (overall easy) direction, indicating FM interaction. These results suggests that in the low temperature ground state, the four Ni ions are oriented in such a way that FM and AFM couplings coexist. Such fine features in the $M(H)$ curves disappears or is averaged out due to thermal fluctuations for temperature above 200 mK, as shown in temperature dependent μSQUID measurements (Fig. S3, ESI†).

2.4. DFT calculations analysis of magnetic interactions

To support the plausibility of the nature and strength of the magnetic interactions, the magnetic coupling for all complexes was theoretically modelled and the spin-density distribution was analyzed. Due to the lack of crystal structures for **1–3**, and to account for possible structural changes due to the halogen substituents on the ligand moieties, the structures of the four complexes were optimized at B3LYP/def2-SVP level. Comparison of the optimized structure of **4** and its experimentally determined geometrical parameters show are in good agreement (see Table S4, ESI†). The calculation of the individual pairwise exchange constants was performed by changing two Ni(II) atoms by two Zn(II) atoms because this method has been probed to give accurate results compared to tetranuclear models.[68,69] The calculated values of the magnetic coupling constant, J were obtained using the broken-symmetry approach[70–73] and the results are gathered in Table 1 and Tables S5 and S6 (ESI†). As observed, the interactions

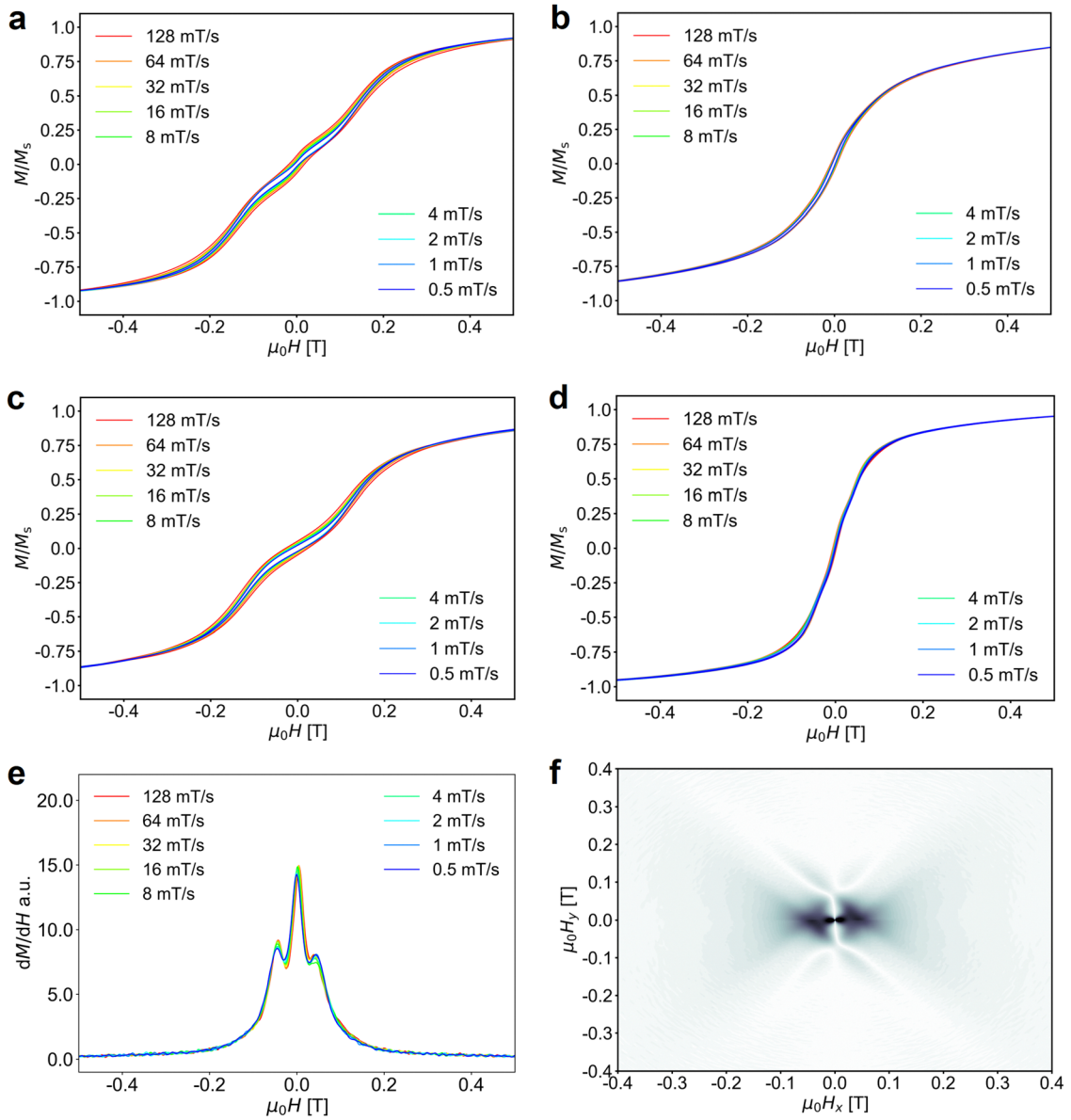

Fig. 7 *M*(*H*) loops for a micron-sized single crystal of (a) **1**; (b) **2**; (c) **3** and (d) **4**, measured by μSQUID at 30 mK bath temperature and different field sweep rates. (e) shows the derivatives d*M*/d*H*(*H*) obtained from the *M*(*H*) loops of complex **4** shown in (d). (f) shows the derivative-field angle map, *i.e.*, d*M*/d*H* mapped with field directions (H_x, H_y).

are found to be ferromagnetic and of the same order for all of them.

$$J = -\frac{E_{HS} - E_{BS}}{S_{max}{}^2} \quad (2)$$

Mulliken spin population analysis calculated for these compounds (see Tables S7–S11, ESI†) shows that although the maximum spin-density is located on the Ni atoms (*ca.* 3.45 e), there is a significant delocalization over the ligands (*ca.* 0.55 e). The unpaired electrons of the octahedral Ni(II)

Table 1 Experimental and theoretical magnetic coupling constants *J* (cm^{-1}) obtained for complexes **1–4**

	J_{exp}		$J_{calculated}$					
Compound	J_1	J_2	Ni(1)–Ni(2)	Ni(1)–Ni(3)	Ni(1)–Ni(4)	Ni(2)–Ni(3)	Ni(2)–Ni(4)	Ni(3)–Ni(4)
1	9.3(6)	0.4(7)	6.58	13.08	13.46	13.47	13.15	6.73
2	6.27(9)	6.26(2)	6.87	12.92	13.28	13.18	12.95	6.88
3	12.5(2)	1.94	7.74	13.10	6439.48	13.46	13.20	7.54
4	32.5(3)	13.8(2)	7.45	12.88	12.95	12.86	12.99	7.74

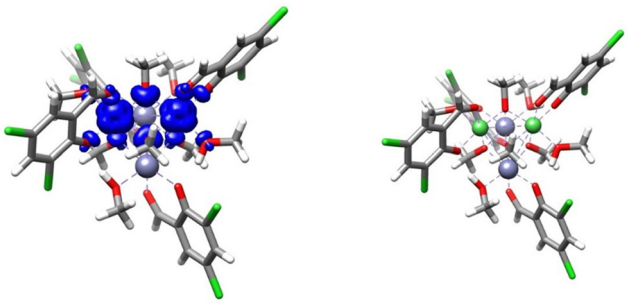

Fig. 8 Graphical representation of the spin density (contour 0.004 e Å^{-3}) at the ground-state (high-spin) configuration (left) and theoretical model used (right) of compound **1**, $\mathbf{J_1}$.

orbitals (d_{z^2} and $d_{x^2\ y^2}$) along with the orbitals of the bridging ligands are involved in the superexchange pathway. Fig. 8 and Fig. S4–S8 (ESI†) collect the spin density plot calculated for complex **1** involving the six combinations of couples of Ni atoms showing the participation of the surrounding oxygen atoms. The contributions to the spin density of the d_{z^2} and $d_{x^2\ y^2}$ orbitals are around 40% for each nickel (see Table S12, ESI†). Analogous comments can be done for the other complexes.

The DFT obtained J values for all compounds lie in two groups. The coupling constants $J_{Ni1\ Ni2}$ and $J_{Ni3\ Ni4}$ display values of around 7 cm^{-1} while the coupling constants of the other combinations of Ni pairs show values around 13 cm^{-1}. The nature and magnitude of the values are in good agreement with the experimental values obtained for J in complexes **2** and **3**. A reasonable agreement can likewise be observed when comparing the interactions found for **1** and considering that the experimentally determined J_2 is antiferromagnetic but very close to zero. In contrast, the data for **4** predicts relatively strong ferromagnetic and antiferromagnetic interactions. Note that, although the crystal structure of complex **4** was the only one experimentally determined, the $\chi_M T(T)$ and $M(H,T)$ fits for this complex are lower compared to the fits for **1–3**. The discrepancies between the experimentally determined and DFT-obtained interaction in this case can be ascribed to the structural distortion of complex **4**.

3. Conclusions

In summary, four tetranuclear cubane-like nickel(II) complexes with general formula $Ni_4(X,Y\text{-}L)_4(\mu_3\text{-}OMe)_4(MeOH)_4$ have been prepared by the reaction of $NiCl_2{\cdot}6H_2O$ with halogen-substituted salicylaldehydes at room temperature to investigate the effects of halogen groups in salicylaldehyde ligand on the magnetic properties. The X-ray crystal structure analysis revealed that **4** has a distorted cubane topology shaped by four bidentate ligands and $[Ni^4(\mu\text{-}O_4)]$ core is formed *via* the O atoms from the methoxy groups. Each Ni(II) ion has a distorted octahedral geometry and is coordinated by three bridging methoxo-oxygens, one oxygen atom from a methanol molecule and two oxygen atoms from the bidentate ligands similar to previous works.[71] Conventional SQUID and μSQUID measurements down to 30 mK bath temperature suggest the co-existence of ferromagnetic and antiferromagnetic couplings among the four Ni ions in the cubane cell. Assessment of the interactions *via* $\chi_M T(T)$ and $M(H,T)$ fits and DFT calculations show that ferromagnetic interactions are operative in all complexes. The observed interactions are in good agreement with the structural considerations, *i.e.*, the Ni–O–Ni angles observed in **4**. While we find a good agreement between the experimentally determined and DFT-determined parameters for **1–3**, the fits and DFT values for **4** have a lower agreement. The differences might arise from geometrical distortions and/or strong intermolecular interactions operating in **4**.

4. Experimental

Materials and general methods

All reagents and solvents for the synthesis and analysis were purchased from commercial sources and used as received. The FT-IR spectra were recorded on a JASCO, FT/IR-6300 spectrometer (4000–400 cm^{-1}) as KBr pellets. The elemental analysis was performed on Leco, CHNS-932 and PerkinElmer 7300 DV elemental analyzers.

Synthesis of complexes

The addition of 10 mmol of $NiCl_2{\cdot}6H_2O$ to a MeOH solution (30 mL) of 3-bromo-5-chlorosalicylaldehyde (10 mmol) and triethylamine (15 mmol) at room temperature yielded a green solution. The reaction mixture was stirred for six hours. The solution was left for slow evaporation of the solvent. Green crystals of the product (Ni–ClBr) formed within several days.

Other complexes were synthesized using identical reaction conditions but yielding precipitates as products. A green precipitate was collected by filtration, washed with methanol, and dried in air.

$[Ni_4(Cl_2\text{-}L)_4(\mu_3\text{-}OMe)_4(MeOH)_4]$ (1). Yield: 85%. Anal. calc. for $C_{37}H_{43}Cl_8Ni_4O_{16}$: C, 35.21; H, 3.43%; found: C, 35.17; H, 3.40%. FT-IR (KBr, cm^{-1}): 3370 ($\nu_{OH\ methanol}$), 1147 ($\nu_{C\ O\ phen}$), 1044 ($\nu_{C\ O\ alcoholic}$).

$[Ni_4(Br_2\text{-}L)_4(\mu_3\text{-}OMe)_4(MeOH)_4]$ (2). Yield: 79%. Anal. calc. for $C_{37}H_{43}Br_8Ni_4O_{16}$: C, 27.47; H, 2.68%; found: C, 27.45; H, 2.65%. FT-IR (KBr, cm^{-1}): 3400 ($\nu_{OH\ methanol}$), 1150 ($\nu_{C\ O\ phen}$), 1046 ($\nu_{C\ O\ alcoholic}$).

$[Ni_4(I_2\text{-}L)_4(\mu_3\text{-}OMe)_4(MeOH)_4]$ (3). Yield: 78%. Anal. calc. for $C_{37}H_{43}I_8Ni_4O_{16}$: C, 22.29; H, 2.17%; found: C, 22.25; H, 2.14%. FT-IR (KBr, cm^{-1}): 3398 ($\nu_{OH\ methanol}$), 1129 ($\nu_{C\ O\ phen}$), 1042 ($\nu_{C\ O\ alcoholic}$).

$[Ni_4(BrCl\text{-}L)_4(\mu_3\text{-}OMe)_4(MeOH)_4]$ (4). Yield: 82%. Anal. calc. for $C_{37}H_{43}Br_4Cl_4Ni_4O_{16}$: C, 30.86; H, 3.01%; found: C, 30.83; H, 2.99%. FT-IR (KBr, cm^{-1}): 3379 ($\nu_{OH\ methanol}$), 1135 ($\nu_{C\ O\ phen}$), 1041 ($\nu_{C\ O\ alcoholic}$).

Single crystal diffraction studies

Single crystal X-ray diffraction data for $[Ni_4(BrCl\text{-}L)_4(\mu_3\text{-}OMe)_4(MeOH)_4]$ (**4**) was collected on a Rigaku OD Synergy/Pilatus

diffractometer using the molybdenum X-ray radiation (λ = 0.71073 Å) from a dual wavelength X-ray source and an Oxford Instruments Cryojet XL cooler. The selected suitable single crystal was mounted using polybutene oil on a flexible loop fixed on a goniometer head and immediately transferred to the diffractometer. Pre-experiment, data collection, data reduction and analytical absorption correction were performed with the program suite *CrysAlisPro*.[74] Using *Olex2*, the structure was solved with the *SHELXT*[75] small molecule structure solution program and refined with the *SHELXL* program package[76] by full-matrix least-squares minimization on F^2. Hydrogen atoms attached to carbon were located in their idealized positions by using appropriate HFIX instructions in SHELXL and included in subsequent refinement cycles in riding-motion approximation with isotropic thermal displacements parameters (U_{iso}) fixed at 1.2 times U_{eq} of the carbon atom to which they are attached. The hydrogen atoms of the –OH group of the methanol molecules were found in difference Fourier maps and refined isotropically. *PLATON*[77] was used to check the result of the X-ray analysis. For more details about the data collection and refinement parameters, see the CIF file.

DFT calculations

DFT calculations were performed using the ORCA 5.0.4 package.[78,79] using the broken-symmetry approach[69 73] as implemented in the software. The level of theory used in this study is B3LYP/def2-SVP which makes use of the hybrid functional B3LYP[80,81] and the basis set def2-SVP for the description of all atoms.[82] The auxiliary def2/J basis set was used to speed up the calculations.[83] Weak interactions were taken into account using the atom-pairwise dispersion correction with the Becke–Johnson damping scheme (D3BJ).[84,85]

Conflicts of interest

There are no conflicts to declare.

Acknowledgements

The authors are grateful to the Research Council of the University of Isfahan (Iran) for financial support of this work. This work is based upon research funded by Iran national science foundation (INSF) under project No. 98024677. We would like to thank the University of Valencia (Spain) for technical assistance in the magnetic measurements. EMP thanks the Panamanian National System of Investigators (SNI) for support. WW thanks the A. v. Humboldt foundation and the ERC grant MoQuOS No. 741276 and DFG-CRC 1573 ''4f for Future''. JVCV thanks the Universidad de Burgos for financial support through the Program of help to the GIRs.

References

1 D. V. Zaytsev, V. A. Morozov, J. Fan, X. Zhu, M. Mukherjee, S. Ni, M. A. Kenned and M. Y. Ogawa, *J. Inorg. Biochem.*, 2013, **119**, 1–9.
2 N. Summa, J. Maigut, R. Puchta and R. Van Eldik, *Inorg. Chem.*, 2007, **46**, 2094–2104.
3 A. Biswas, L. K. Das, M. G. B. Drew, C. Diaz and A. Ghosh, *Inorg. Chem.*, 2012, **51**, 10111–10121.
4 L. Wan, C. Zhang, Y. Xing, Z. Li, N. Xing, L. Wan and H. Shan, *Inorg. Chem.*, 2012, **51**, 6517–6528.
5 S. Bhattacharya, M. Gnanavel, A. J. Bhattacharyya and S. Natarajan, *Cryst. Growth Des.*, 2014, **14**, 310–325.
6 T. N. Nguyen, W. Wernsdorfer, K. A. Abboud and G. Christou, *J. Am. Chem. Soc.*, 2011, **133**, 20688–20691.
7 K. S. Pedersen, J. Bendix and R. Clérac, *Chem. Commun.*, 2014, **50**, 4396–4415.
8 K. Liu, W. Shi and P. Cheng, *Coord. Chem. Rev.*, 2015, **289–290**, 74–122.
9 L. Rosado Piquer and E. C. Sañudo, *Dalton Trans.*, 2015, **44**, 8771–8780.
10 X. F. Ma, Z. Wang, X. L. Chen, M. Kurmoo and M. H. Zeng, *Inorg. Chem.*, 2017, **56**, 15178–15186.
11 T. Ama, M. M. Rashid, T. Yonemura, H. Kawaguchi and T. Yasui, *Coord. Chem. Rev.*, 2000, **198**, 101–116.
12 C. J. Matthews, K. Avery, Z. Xu, L. K. Thompson, L. Zhao, D. O. Miller, K. Biradha, K. Poirier, M. J. Zaworotko, C. Wilson and A. E. Goeta, *Inorg. Chem.*, 1999, **38**, 5266–5276.
13 Y. L. Zhou, M. H. Zeng, X. C. Liu, H. Liang and M. Kurmoo, *Chem. – Eur. J.*, 2011, **17**, 14084–14093.
14 K. Isele, F. Gigon, A. F. Williams, G. Bernardinelli, P. Franz and S. Decurtins, *Dalton Trans.*, 2007, 332–341.
15 M. L. Tong, S. L. Zheng, J. X. Shi, Y. X. Tong, H. K. Lee and X. M. Chen, *J. Chem. Soc., Dalton Trans.*, 2002, 1727–1734.
16 D. Venegas-Yazigi, J. Cano, E. Ruiz and S. Alvarez, *Phys. B*, 2006, **384**, 123–125.
17 R. A. Layfield, *Organometallics*, 2014, **33**, 1084–1099.
18 M. Dey and M. Gogoi, *Angew. Chem., Int. Ed.*, 2013, **52**, 12780–12782.
19 L. Bogani and W. Wernsdorfer, *Nat. Mater.*, 2008, **7**, 179–186.
20 T. Glaser, *Chem. Commun.*, 2011, **47**, 116–130.
21 M. Affronte, F. Troiani, A. Ghirri, A. Candini, M. Evangelisti, V. Corradini, S. Carretta, P. Santini, G. Amoretti, F. Tuna and G. Timco, *J. Phys. D: Appl. Phys.*, 2007, **40**, 2999–3004.
22 A. Enders, R. Skomski and J. Honolka, *J. Phys.: Condens. Matter*, 2010, **22**, 433001.
23 J. S. Miller, *Dalton Trans.*, 2006, 2742–2749.
24 L. Ballester, E. Coronado, A. Gutierrez, A. Monge, M. F. Perpinan, E. Pinilla and T. Rico, *Inorg. Chem.*, 1992, **31**, 2053–2056.
25 W. L. Gladfelter, M. W. Lynch, W. P. Schaefer, D. N. Hendrickson and H. B. Gray, *Inorg. Chem.*, 1981, **20**, 2390–2397.
26 F. Paap, E. Bouwman, W. L. Driessen, R. A. G. de Graaff and J. Reedijk, *J. Chem. Soc., Dalton Trans.*, 1985, 737–741.
27 V. V. Pavlishchuk, S. V. Kolotilov, A. W. Addison, M. J. Prushan, D. Schollmeyer, L. K. Thompson, T. Weyhermüller and E. A. Goreshnik, *Dalton Trans.*, 2003, 1587–1595.
28 A. J. Blake, E. K. Brechin, A. Codron, R. O. Gould, C. M. Grant, S. Parsons, J. M. Rawson and R. E. Winpenny, *J. Chem. Soc., Chem. Commun.*, 1995, 1983–1984.

29 G. Aromi, S. Parsons, W. Wernsdorfer, E. K. Brechin and E. J. L. McInnes, *Chem. Commun.*, 2005, 5038–5040.
30 J. M. Clemente-Juan, B. Chansou, B. Donnadieu and J. P. Tuchagues, *Inorg. Chem.*, 2000, **39**, 5515–5519.
31 M. A. Halcrow, J. S. Sun, J. C. Huffman and G. Christou, *Inorg. Chem.*, 1995, **34**, 4167–4177.
32 B. A. Breeze, M. Shanmugam, F. Tuna and R. E. P. Winpenny, *Chem. Commun.*, 2007, 5185–5187.
33 D. Ruiz-Molina, M. Mas-Torrent, J. Gómez, A. I. Balana, N. Domingo, J. Tejada, M. T. Martínez, C. Rovira and J. Veciana, *Adv. Mater.*, 2003, **15**, 42–45.
34 P. L. Feng, C. J. Stephenson and D. N. Hendrickson, *Inorg. Chem.*, 2010, **49**, 6393–6395.
35 M. Atanasov, B. Delley, F. Neese, P. L. Tregenna-Piggott and M. Sigrist, *Inorg. Chem.*, 2011, **50**, 2112–2124.
36 S. H. Zhang, Y. Song, H. Liang and M. H. Zeng, *CrystEngComm*, 2009, **11**, 865–872.
37 E. C. Jose, R. S. Fraser, J. White and E. K. Brechin, *Inorg. Chem.*, 2011, **50**, 7268–7273.
38 S. H. Zhang, N. Li, C. M. Ge, C. Feng and L. F. Ma, *Dalton Trans.*, 2011, **40**, 3000–3007.
39 T. Jurca, A. Farghal, P. H. Lin, I. Korobkov, M. Murugesu and D. S. Richeson, *J. Am. Chem. Soc.*, 2011, **133**, 15814–15817.
40 S. H. Zhang, L. F. Ma, H. H. Zou, Y. G. Wang and H. Liang, *Dalton Trans.*, 2011, **40**, 11402–11409.
41 H. Q. Tian, Y. N. Guo, L. Zhao, J. K. Tang and Z. L. Liu, *Inorg. Chem.*, 2011, **50**, 8688–8690.
42 Y. N. Guo, G. F. Xu, W. Wernsdorfer, L. Ungur, Y. Guo, J. Tang, H. J. Zhang, L. F. Chibotaru and A. K. Powell, *J. Am. Chem. Soc.*, 2011, **133**, 11948–11951.
43 H. Miyasaka, K. Nakata, L. Lecren, C. Coulon, Y. Nakazawa, T. Fujisaki, K. I. Sugiura, M. Yamashita and R. Clérac, *J. Am. Chem. Soc.*, 2006, **128**, 3770–3783.
44 S. H. Zhang, Y. L. Zhou, X. J. Sun, L. Q. Wei, M. H. Zeng and H. Liang, *J. Solid State Chem.*, 2009, **182**, 2991–2996.
45 Y. Song, P. Zhang, X. M. Ren, X. F. Shen, Y. Z. Li and X. Z. You, *J. Am. Chem. Soc.*, 2005, **127**, 3708–3709.
46 (*a*) C. Y. Qin, S. Z. Zhao, H. W. Zhou, Y. H. Li and S. Wang, *Polyhedron*, 2022, **222**, 115896; (*b*) R. T. Marques, F. F. Martins, D. F. Bekiş, A. I. Vicente, L. P. Ferreira, C. S. Gomes, S. Barroso, V. Kumar, Y. Garcia, N. A. Bandeira and M. J. Calhorda, *Magnetochemistry*, 2022, **8**, 162.
47 R. Liu, C. Zhang, L. Li, D. Liao and J. P. Sutter, *Dalton Trans.*, 2012, **41**, 12139–12144.
48 S. K. Langley, D. P. Wielechowski, B. Moubaraki and K. S. Murray, *Chem. Commun.*, 2016, **52**, 10976–10979.
49 S. K. Langley, D. P. Wielechowski, V. Vieru, N. F. Chilton, B. Moubaraki, L. F. Chibotaru and K. S. Murray, *Chem. Sci.*, 2014, **5**, 3246–3256.
50 W. Phonsri, D. S. Macedo, B. Moubaraki, J. D. Cashion and K. S. Murray, *Magnetochemistry*, 2016, **2**, 3.
51 W. Phonsri, D. S. Macedo, K. R. Vignesh, G. Rajaraman, C. G. Davies, G. N. Jameson, B. Moubaraki, J. S. Ward, P. E. Kruger, G. Chastanet and K. S. Murray, *Chem. – Eur. J.*, 2017, **23**, 7052–7065.
52 W. Phonsri, C. G. Davies, G. N. Jameson, B. Moubaraki, J. S. Ward, P. E. Kruger, G. Chastanet and K. S. Murray, *Chem. Commun.*, 2017, **53**, 1374–1377.
53 R. Biswas, Y. Ida, M. L. Baker, S. Biswas, P. Kar, H. Nojiri, T. Ishida and A. Ghosh, *Chem. – Eur. J.*, 2013, **19**, 3943–3953.
54 M. Aryaeifar, H. A. Rudbari and G. Bruno, *Polyhedron*, 2018, **155**, 114–128.
55 H. A. Rudbari, F. Lloret, M. Khorshidifard, G. Bruno and M. Julve, *RSC Adv.*, 2016, **6**, 7189–7194.
56 N. Kordestani, H. A. Rudbari, G. Bruno, S. Rosario, J. D. Braun, D. E. Herbert, O. Blacque, I. Correia, M. A. M. Zaman, M. M. Bindu and C. Janiak, *Dalton Trans.*, 2020, **49**, 8247–8264.
57 M. J. Turner, J. J. McKinnon, S. K. Wolff, D. J. Grimwood, P. R. Spackman, D. Jayatilaka and M. A. Spackman, *CrystalExplorer17*, University of Western Australia, Crawley, WA, Australia, 2017.
58 J. J. McKinnon, M. A. Spackman and A. S. Mitchell, *Acta Crystallogr., Sect. B: Struct. Sci.*, 2004, **60**, 627.
59 M. A. Spackman and J. J. McKinnon, *CrystEngComm*, 2002, **4**, 378–392.
60 J. J. McKinnon, D. Jayatilaka and M. A. Spackman, *Chem. Commun.*, 2007, 3814–3816.
61 P. R. Spackman, M. J. Turner, J. J. McKinnon, S. K. Wolff, D. J. Grimwood, D. Jayatilaka and M. A. Spackman, *J. Appl. Crystallogr.*, 2021, **54**, 1006–1011.
62 A. V. Bondi, *J. Phys. Chem.*, 1964, **68**, 441–451.
63 J. P. Costes, G. Novitchi, L. Vendier, G. Pilet and D. Luneau, *C. R. Chim*, 2012, **15**, 849–855.
64 Z. You, Y. Luo, S. Herringer, Y. Li, S. Decurtins, K. W. Krämer and S. X. Liu, *Crystals*, 2020, **10**, 592.
65 F. Kobayashi, R. Ohtani, S. Teraoka, W. Kosaka, H. Miyasaka, Y. Zhang, L. F. Lindoy, S. Hayami and M. Nakamura, *Dalton Trans.*, 2017, **46**, 8555–8561.
66 Q. L. Zhang, Z. L. Wu, H. Xu, B. Zhai, Y. F. Wang, G. W. Feng and Y. L. Huang, *Z. Anorg. Allg. Chem.*, 2016, **642**, 414–418.
67 N. F. Chilton, R. P. Anderson, L. D. Turner, A. Soncini and K. S. Murray, *J. Comput. Chem.*, 2013, **34**, 1164–1175.
68 M. Pait, A. Bauzá, A. Frontera, E. Colacio and D. Ray, *Inorg. Chem.*, 2015, **54**, 4709–4723.
69 E. Ruiz, A. Rodríguez-Fortea, J. Cano, S. Alvarez and P. Alemany, *J. Comput. Chem.*, 2003, **24**, 982–989.
70 L. Noodleman, *J. Chem. Phys.*, 1981, **74**, 5737–5743.
71 A. P. Ginsberg, *J. Am. Chem. Soc.*, 1980, **102**, 111–117.
72 L. Noodleman and E. R. Davidson, *Chem. Phys.*, 1986, **109**, 131–143.
73 E. Ruiz, J. Cano, S. Alvarez and P. Alemany, *J. Comput. Chem.*, 1999, **20**, 1391–1400.
74 *CrysAlisPro (version 1.171.42.57a)*, Rigaku Oxford Diffraction Ltd, Yarnton, Oxfordshire, England, 2022.
75 G. M. Sheldrick, SHELXT - Integrated space-group and crystal-structure determination, *Acta Crystallogr., Sect. A: Found. Adv.*, 2015, **71**, 3.
76 G. M. Sheldrick, Crystal structure refinement with SHELXL, *Acta Crystallogr., Sect. C: Struct. Chem.*, 2015, **71**, 3.

77 A. L. Spek, Structure validation in chemical crystallography, *Acta Crystallogr., Sect. D: Biol. Crystallogr.*, 2009, **65**, 148.
78 F. Neese, *Wiley Interdiscip. Rev.: Comput. Mol. Sci.*, 2012, **2**, 73–78.
79 F. Neese, *Wiley Interdiscip. Rev.: Comput. Mol. Sci.*, 2022, **12**, e1606.
80 A. D. Becke, *J. Chem. Phys.*, 1993, **98**, 5648–5652.
81 C. T. Lee, W. T. Yang and R. G. Parr, *Phys. Rev. B: Condens. Matter Mater. Phys.*, 1988, **37**, 785–789.
82 F. Weigend and R. Ahlrichs, *Phys. Chem. Chem. Phys.*, 2005, **7**, 3297–3305.
83 F. Weigend, *Phys. Chem. Chem. Phys.*, 2006, **8**, 1057–1065.
84 S. Grimme, J. Antony, S. Ehrlich and H. Krieg, *J. Chem. Phys.*, 2010, 132.
85 S. Grimme, S. Ehrlich and L. Goerigk, *J. Comput. Chem.*, 2011, **32**, 1456–1465.